

## Effect of reinforcement strength on seismic behavior of concrete moment frames

Jianping Fu<sup>1a</sup>, Yuntian Wu<sup>\*1</sup> and Yeong-bin Yang<sup>1,2b</sup>

<sup>1</sup>Lab for construction of mountainous city and new technology of Ministry of education of China, School of Civil Engineering, 83 Shazheng Street, Shapingba District, Chongqing 400045, China

<sup>2</sup>Department of Civil Engineering, National Taiwan University, No.1, Sec.4, Roosevelt Road, Taipei 10617, Taiwan

(Received December 17, 2014, Revised July 20, 2015, Accepted July 22, 2015)

**Abstract.** The effect of reinforcing concrete members with high strength steel bars with yield strength up to 600 MPa on the overall seismic behavior of concrete moment frames was studied experimentally and numerically. Three geometrically identical plane frame models with two bays and two stories, where one frame model was reinforced with hot rolled bars (HRB) with a nominal yield strength of 335 MPa and the other two by high strength steel bars with a nominal yield strength of 600 MPa, were tested under simulated earthquake action considering different axial load ratios to investigate the hysteretic behavior, ductility, strength and stiffness degradation, energy dissipation and plastic deformation characteristics. Test results indicate that utilizing high strength reinforcement can improve the structural resilience, reduce residual deformation and achieve favorable distribution pattern of plastic hinges on beams and columns. The frame models reinforced with normal and high strength steel bars have comparable overall deformation capacity. Compared with the frame model subjected to a low axial load ratio, the ones under a higher axial load ratio exhibit more plump hysteretic loops. The proved reliable finite element analysis software DIANA was used for the numerical simulation of the tests. The analytical results agree well with the experimental results.

**Keywords:** high strength; reinforcement; moment frame; seismic performance; plastic hinge

### 1. Introduction

The steel reinforcement with yield strength in excess of 550 MPa is generally regarded as high strength steel reinforcement, which has not been documented in most building codes in the world. It has been widely accepted, however, that increasing the strength of steel reinforcement can provide many practical advantages to the concrete construction industry. The cross sectional size and quantity of reinforcement of concrete members can be reduced resulting in savings in material, shipping and labor costs. The steel congestion problem of heavily reinforced concrete columns can be addressed by using high strength longitudinal reinforcing bars. The associated use of high

---

\*Corresponding author, Associate Professor, E-mail: [yuntianw@cqu.edu.cn](mailto:yuntianw@cqu.edu.cn)

<sup>a</sup>Professor, E-mail: [fjp@cqu.edu.cn](mailto:fjp@cqu.edu.cn)

<sup>b</sup>Professor, E-mail: [ybyang@ntu.edu.tw](mailto:ybyang@ntu.edu.tw)

strength steel reinforcement with high strength concrete can yield a more efficient use of both materials. Many high strength grades of reinforcement can provide enhanced corrosion resistance compared with conventional reinforcing steel.

The recent development of concrete design codes in many countries has exhibited the trend of increasing the yield strength of reinforcement for design of concrete members. In the United States, the permitted reinforcement strength has been increased from 414 MPa to 550 MPa (ACI 318-71). A National Cooperative Highway Research Program (NCHRP) Project was initiated in 2007 to evaluate the AASHTO LRFD bridge design specifications (AASHTO 2002) with respect to the use of high strength reinforcing steel and other grades of reinforcing steel having no discernable yield plateau, leading to a number of recommendations that were subsequently incorporated into the 2013 interim revisions of the AASHTO specifications (AASHTO 2013) to permit the use of high strength reinforcing steel with specified yield strengths greater than 517 MPa. In China, the longitudinal reinforcing bars used in design of concrete structures were dominated by hot rolled bars (HRB) having nominal yield strength,  $f_y$ , equal to 335 MPa (HRB335) for many years and since about 2002 having nominal yield strength equal to 400 MPa (HRB400). In the current Chinese Code for Design of Concrete Structures (GB50010-2010) the permitted value of yield strength is further increased to 500 MPa (HRB500). By far HRB500 reinforcement has become more and more widely used in China.

Research on the use of high strength steel reinforcement for concrete construction has been ongoing for a long time. In addition to the aforementioned NCHRP project, various researchers conducted analytical and experimental studies on key issues such as the flexural capacity calculation, crack control and deformation characteristics of concrete members using high strength reinforcement with specified yield strength up to or even higher than 689 MPa. Mast *et al.* (2008) presented a methodology for the flexural strength design of concrete beams reinforced with high strength reinforcing bars. Harries *et al.* (2012) investigated the flexural crack widths of flexural members with high strength reinforcement up to 827 MPa and concluded that the ACI and AASHTO provisions for crack control can be extended to be used for flexural beams with high strength reinforcement. Shahrooz *et al.* (2013) demonstrated that in order to achieve comparable curvature ductility to that implicit with the use of the ASTM Grade 60 reinforcement the strain limits for high strength reinforcement must be changed. On the other hand, the seismic performance of concrete structures reinforced with high strength steel has attracted more and more attention of researchers and practicing engineers in that most of the regions having intention to widely use high strength reinforcement are subjected to seismic risk. It has been most concerned about the possible inadequate ductility of concrete members utilizing high strength reinforcing steel caused by the use of larger yield stress. Due to the lack of research background, current building codes in many countries contain stringent provisions regarding the reinforcement strength that can be used in the design of seismic force resisting concrete structures. For earthquake-resistant design ACI 318 (2011) specifies the longitudinal reinforcement of Grade 60 (410 MPa) or lower. The Chinese Code for Seismic Design of Buildings (GB 50011-2010) also requires that the reinforcement for seismic force resisting concrete structures possess a ratio of measured tensile strength to measured yield strength no less than 1.25 and a total elongation rate no less than 9% under the maximum tensile force. These provisions are intended to ensure the ductile behavior of concrete structures under earthquake ground motions based on the ductility measure defined as the ratio of ultimate deformation to that at yield condition, where the deformation can be taken as sectional curvature, deflection and inter-story drift, etc. Rautenberg *et al.* (2012) found that the concrete column with high strength steel reinforcement can be designed

to obtain the deformation capacity and flexural strength comparable to those of concrete columns reinforced with ASTM Grade 60 steel bars. Wang (2013) demonstrated that the ductility demand of concrete columns with high strength reinforcement is lower than that of concrete columns with normal strength reinforcement, and both types of columns show similar overall seismic performance in terms of strength and total deformation. Fu *et al.* (2014) conducted nonlinear dynamic analysis on four moment frames with high strength reinforcement and one moment frame with normal strength reinforcement to investigate the dynamic responses of moment frames with various strength of reinforcement under different levels of earthquake ground motions. The analysis results indicate the moment frames using high strength reinforcement can be designed to achieve overall dynamic behavior similar to that of frames with normal strength reinforcement. It can be easily seen, however, that previous studies mainly focused on the behavior of concrete members and have rarely dealt with the effect of reinforcement strength on the overall seismic behavior of concrete structures such as moment resisting frames in terms of failure pattern, yield sequence, strength and stiffness degradation characteristics. Although the conventional ductility measure does not favor the use of high strength reinforcement in seismic regions, more research background is needed to demonstrate that the high strength reinforcement can also ensure safe and reliable performance of concrete structures located in seismic regions. In addition, recent disastrous earthquakes in China such as the Wenchuan Earthquake in 2008 have illustrated the considerable difficulty in rehabilitation of damaged concrete buildings caused by the excessive post-yield and residual deformation (Civil and Structural Groups 2008). For concrete buildings subjected to earthquake ground motions of significant intensity, the structural resilience is very important for the safety and post-quake rehabilitation. It is believed by many researchers that the larger yield stresses of high strength reinforcement and the subsequent greater utilization of concrete capacity may be beneficial to the structural resilience by reduction of post-yield and residual deformation of concrete structures provided that sufficient total deformation capacity of the structure is ensured.

In this research program, tests of three two-bay and two-story plane moment frame models with the consideration of slab were conducted. One test frame model was reinforced using HRB335 normal strength steel bars while the other two using HRB600 high strength steel bars. The seismic performance of the three test models were systematically studied in terms of hysteretic behavior, ductility, stiffness degradation, deformation restoring capacity and rotation of plastic hinges. Nonlinear finite element analysis was also carried out to verify the experimental results.

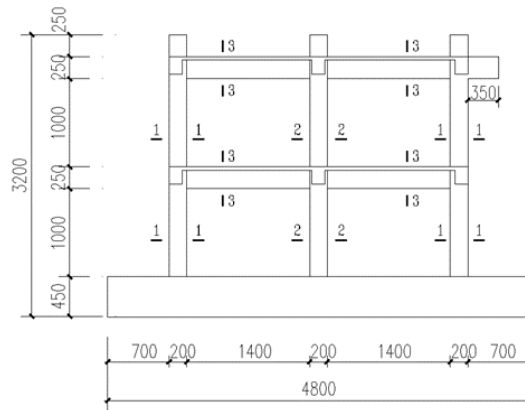
## 2. Experimental program

### 2.1 Test frame models

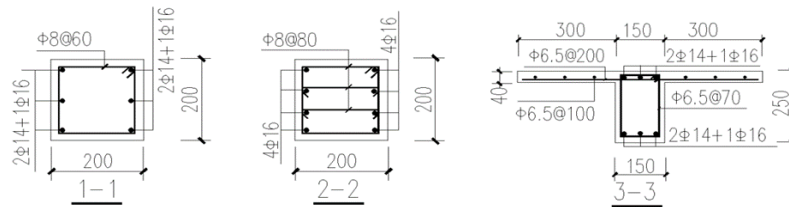
The two-story and two-bay frame models tested in this research program were identified by TF-1, TF-2 and TF-3 respectively and designed in accordance with The Chinese Code for Seismic Design of Buildings (GB 50011-2010). All the three test frame models were 1:3 scaled and had identical overall dimensions. The total height of each model was 3200 mm with a typical story height of 1250 mm. The typical bay width was 1600 mm. The cross sectional dimensions were 150 mm×250 mm and 200 mm×200 mm for beams and columns respectively. For test model TF-1, the beams were reinforced with two No. 14 and one No. 16 HRB335 normal strength steel bars on the top and bottom sides of cross section respectively. The exterior columns were reinforced with four

Table 1 Test matrix

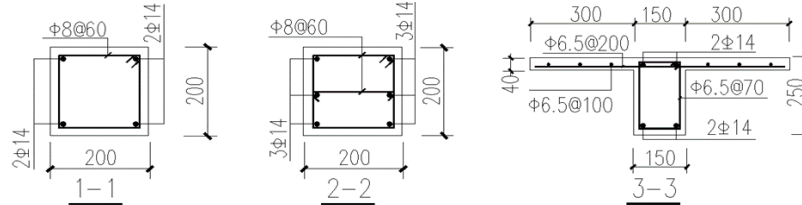
Identification	Longitudinal reinforcement	Axial compression ratio	
		Interior column	Exterior column
TF-1	HRB335	0.2	0.1
TF-2	HRB600	0.2	0.1
TF-3	HRB600	0.45	0.15



(a) Overall dimensions of specimens



(b) Cross-sectional dimensions and reinforcement of TF-1



(c) Cross-sectional dimensions and reinforcement of TF-2 and TF-3

Fig. 1 Details of test frame models

No. 14 and two No. 16 HRB335 normal strength steel bars. The interior columns were reinforced with eight No. 16 steel bars. For test models TF-2 and TF-3, the beams were reinforced with two No. 14 HRB600 high strength steel bars on both top and bottom sides of cross section. The exterior and interior columns were reinforced with four No. 14 and six No. 14 HRB600 high strength steel bars respectively. The geometrical dimensions and amounts of reinforcement used for the members of frame models TF-1, TF-2 and TF-3 were determined based on the rule that

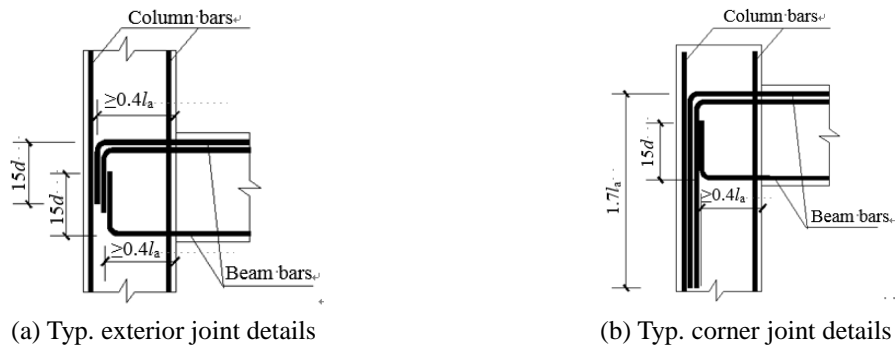


Fig. 2 Details of typical beam-column joints

member cross sections reinforced with various strength steel bars obtain similar, if not identical, load carrying capacity and stiffness in magnitude so as to make the three test frame models comparable to each other in the aspect of strength design. The contribution of slab to the flexural resistance and stiffness of beams was considered by including an extra 40 mm×300 mm overhanging flange on both sides of the beam. And uniformly distributed reinforcing bars were provided for the overhung beam flanges. For the convenience of applying axial load during tests, each column of the frame model was further extended beyond the top story to form a 250 mm-tall stub column, to which the hydraulic jack will be connected. The beam on the top story of each frame model was also extended beyond the exterior beam-column joint for 350 mm and enlarged in cross section with increased amount of reinforcement for strengthening, where the horizontal actuator was then connected through the embedded high-strength threaded rods. Fig. 1 depicts the details of the test frame models. The typical reinforcement details of beam-column joint regions are shown in Fig. 2, where  $d$  is the nominal diameter of longitudinal rebars,  $l_a$  is the anchorage length calculated in accordance with the provisions in GB 500011-2010.

Another parameter considered in tests was the axial compressive load ratio, which was defined as the ratio of the applied axial load  $N$  to the axial compressive capacity of the column section,  $f'_c b h$ , where  $f'_c$  is the compressive strength of concrete measured on the date of testing;  $b$  and  $h$  are the width and depth of the column cross section. To reflect the actual condition, the interior and exterior columns of each test moment frame were compressed following different axial load ratios. The axial load ratios for exterior and interior columns of frame models TF-1 and TF-2 were 0.1 and 0.2 respectively while those of frame model TF-3 were 0.15 and 0.45 respectively. The matrix showing the main test parameters of the three frame models is given in Table 1. The test results of TF-1 and TF-2 were used to study the influence of reinforcement strength on the performance of frame models under the same axial load ratio and those of TF-2 and TF-3 were used to examine the effect of axial load ratio on frame models using high strength reinforcement.

## 2.2 Test setup and loading protocol

The tests were carried out at the structural laboratory of Chongqing University. In addition to the constant axial loads applied on top of the columns, the frame models were horizontally loaded at the top story to simulate the lateral displacement reversals caused by earthquake ground motion. The axial load was applied to each column by vertical hydraulic jacks with a maximum load

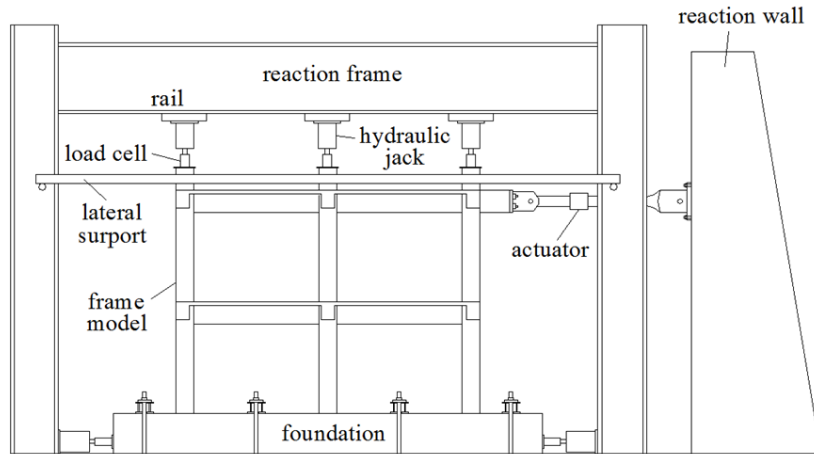


Fig. 3 Test setup

Table 2 Peak values of inter-story drift angle  $\theta$  for horizontal loading procedure

Step	0	1	2	3	4	5	6	7	8	9	10	11	12	13
$\theta$	$\frac{1}{1500}$	$\frac{1}{1200}$	$\frac{1}{800}$	$\frac{1}{600}$	$\frac{1}{400}$	$\frac{1}{300}$	$\frac{1}{200}$	$\frac{1}{150}$	$\frac{1}{100}$	$\frac{1}{75}$	$\frac{1}{55}$	$\frac{1}{40}$	$\frac{1}{30}$	$\frac{1}{25}$

capacity of 500 kN. The cyclic horizontal load was applied by a two-way servo-controlled hydraulic actuator with a maximum loading capacity of 1000 kN and a stroke of  $\pm 250$  mm. The vertical hydraulic jack can slide horizontally along a specially designed steel rail installed on the bottom flange of the reaction beam against which the axial load was applied. Thus the axial loading to each column can be maintained as the frame models deflect horizontally during the test. Lateral restraint for preventing out of plane deformation of the test frame model was also provided by two relatively rigid steel shape beams on the top story level of frame models. Teflon pads were used between the restraining beams and the frame model to reduce the friction that may be mobilized when the frame laterally displaces during the loading procedure. During the test, the contraction and extension of the horizontal actuator were taken as the positive (+) and negative (-) loading directions respectively. The test setup was shown in Fig. 3. Axial loads were applied prior to the commencement of lateral loading and maintained approximately constant during the testing. The increments within the lateral load cycles were controlled by inter-story drift angle,  $\theta$ , defined as the ratio between the relative horizontal displacement measured by the displacement transducer horizontally mounted on top floor level and the total height of the model. The lateral load sequence consisted of two cycles to each inter-story drift angle,  $\theta$ , of the values given in Table 2. If the instant lateral load carrying capacity of the test frame model degrades below 85% of its measured peak load carrying capacity, the test would be terminated. However, if the test frame model is laterally displaced so large that the vertical hydraulic jacks cannot further move horizontally due to the limited rail length, the test will be terminated too.

### 2.3 Instrumentation

The instrumentation plan was designed to measure the yield sequence and the rotational

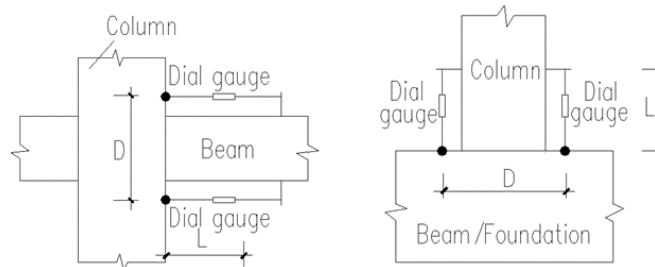


Fig. 4 Dial gauge arrangement for rotation measurement

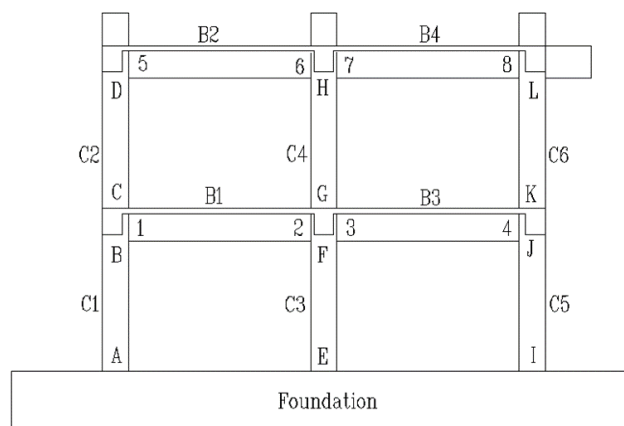


Fig. 5 Identification of control sections of test frame models

behavior of beam and column ends during tests. Strain gages were mounted on four corner longitudinal reinforcing bars at beam and column end sections. The flexural rotation of beam and column end regions was measured by dial gages installed on both sides of the member along the assumed plastic hinge length. Let  $\Delta_1$  and  $\Delta_2$  be the elongation on the outer face in tension and the shortening on the outer face in compression measured between the mounting location of dial gage and the surface of intersecting member face, then the corresponding rotation can be approximated by

$$\phi = \frac{|\Delta_1| + |\Delta_2|}{D} \tag{1}$$

where  $\phi$  is the average rotational angle;  $D$  is the distance between the dial gages mounted on the two sides of the member. Fig. 4 illustrates the typical arrangement of dial gages. The monitored beam and column end regions are numbered in Fig. 5 for reference in the discussion of test results.

### 2.4 Material properties

The concrete used for all three test models was C40 with specified cubic compressive strength of 40 MPa based on 150 mm×150 mm×150 mm standard cubic samples. The actual average concrete compressive strength of the three test models on the days of testing were 38.5 MPa, 39.8 MPa and 36.5 MPa respectively calculated based on the standard cubic samples. The longitudinal

reinforcing bars used in TF-1 were HRB335 14 mm and 16 mm diameters deformed bars and those in TF2 and TF3 were HRB600 14 mm diameter deformed bars. The steel coupon test results indicated an average yield strength of 436.6 MPa and 425.2 MPa for HRB335 14 mm and 16 mm diameters deformed bars respectively and 659.4 MPa for HRB600 14 mm diameter deformed bars.

### 3. Experimental observations and discussion

#### 3.1 General observations

At the initial loading stage, the horizontal load applied to test frames was small, resulting in an approximately linear lateral load-displacement relationship. Only very few minute cracks were detected in some of the frame beams while the rest beams and columns remained intact. Starting from the inter-story drift angle of 1/800, cracks at bottom of beam end sections were observed caused by positive bending moment then followed by the cracking at top of beam end sections and slab caused by negative bending moment. The presence of slab increased the modulus of rupture of the section under negative bending moment, resulting in the earlier cracking at bottom of beam end than top of beam end. When the inter-story drift angle reached 1/600, the columns of test frame models TF-1 and TF-2 started to crack at bottom end regions. The columns of test frame model TF-3 began to crack when the inter-story drift angle reached 1/300 due to its higher axial load ratio.

The yielding condition of test frame models was monitored using the readings of strain gages attached to the longitudinal reinforcing bars. For test frame model TF-1, which was reinforced with normal strength steel bars, the beam end section at location 1 yielded first and then other beam and column end sections started to yield corresponding to the inter-story drift angle of 1/100. Under the same inter-story drift angle, however, yielding only occurred at one beam end section in test frame models TF-2 and TF-3 respectively and no column section yielded due to their use of high strength reinforcement. Along with the further increase of inter-story drift angle, more and more beams and columns yielded and the lateral stiffness gradually degraded. In the positive and negative loading directions corresponding to the inter-story drift angle of 1/55, test frame model TF-1 reached its peak lateral capacity of 235.3 kN and 258.7 kN respectively. Test frame model TF-2 arrived at its peak lateral load capacity of 256.2 kN in the positive loading direction corresponding to the inter-story drift angle of 1/40. Its peak lateral load capacity of 235.8 kN in the negative loading direction was reached corresponding to the inter-story drift angle of 1/55. For the test frame model TF-3, the peak lateral load capacity of 266.3 kN in the positive loading direction was reached corresponding to the inter-story drift angle of 1/50 and that of 237.7 kN in the negative direction was reached corresponding to the inter-story drift angle of 1/55. It can be seen that the three test frame models designed based on the capacity equivalence rule exhibited similar lateral load carrying capacity even if various strength of reinforcements were used. The peak lateral strength of TF-3 was slightly higher than those of TF-1 and TF-2 due to the higher axial load ratio.

After the test frame models reached their peak lateral strength, the lateral load-displacement relationship started to descend. The tests of all three test frame models were concluded corresponding to the inter-story drift angle of 1/25, since the vertical hydraulic jacks had arrived at its limits for further lateral movement. The lateral load carrying capacities of all three frame models were still above 85% of the peak capacities when the tests were concluded. The ultimate



(a) Beam end 4, TF-1



(b) Beam end 2, TF-2



(c) Beam end 3, TF-3

Fig. 6 Damages at beam ends



(a) Column bottom end E, TF-1



(b) Column bottom end E, TF-2



(c) Column bottom end E, TF-3

Fig. 7 Damages at column ends

failure patterns of the test frame models indicated the significant influence of slab. Firstly, cracking of the bottom side of beam end section without slab was much earlier than that of the top side of beam end section with slab. Secondly, the ultimate damages to the beam ends concentrated at the bottom side of the beam end sections. Fig. 6 shows the typical damage condition at beam ends of the three test frame models. It was also observed that only few minor cracks appeared at the beam-column joint regions in all three frame models during the tests. Cracking and formation of plastic hinges at beam ends were earlier than those at column ends. For test frame model TF-3, plastic hinges at column ends were further postponed compared with the other two frame models due to its higher axial load ratio. The spalling off of concrete at bottom story column end regions of TF-3 was much severe than frame models TF-1 and TF-2. The ultimate damage conditions for the three test frames models are exhibited in Fig. 7.

### 3.2 Yield sequence and plastic hinge development

Although all the three test frame models developed a mixed beam and column hinging pattern when the tests were terminated, their yield sequences and proportions of column hinges varied, reflecting the influences of reinforcement strength and axial load ratio. Plastic hinges formed at all beam ends of test frame models, except for beam end 8 where strengthening was provided for the sake of horizontal loading application. According to the experimental observations, the yield sequences of the test frame models can be explained in three levels. Firstly, the bottom side of each

Table 3 Yield sequence of members of test frame models

$\theta$	TF-1		TF-2		TF-3	
	+ loading	-loading	+ loading	-loading	+loading	-loading
1/200	—	—	—	—	—	—
1/150	—	4	—	—	—	—
1/100	4, 1, 2, K, A	1, 3, 5, K, A, E	4	2	2	3
1/75	E, N	7, N, D	1, C	4, A	4, 6	1
1/55	5, H	2, H	2, E, K	D	—	—
1/50	—	—	—	—	7, 3	5, 2
1/40	3, M, G	6, B, C	A, N	3, E	E, K	E, A
1/30	F	—	H, K	5, H, N	A	K

beam end typically yielded prior to the top side due to the presence of slab. Secondly, the cracking and member yielding were typically initiated from beam ends and along with the loading column ends gradually developed plasticity. Thirdly, compared with test frame model TF-1 which utilized normal strength reinforcement, frame models TF-2 and TF-3 using high strength reinforcing bars started to yield corresponding to larger inter-story drift angles and fewer column plastic hinges were developed. As of the frame model TF-3 which was subjected to higher axial load than the other two models, the number of plastic hinges was further reduced. Table 3 shows the yield sequences of the member end sections of all three frame models. It can be seen that at the same inter-story drift angle, the total number of yielded members of the models with high strength reinforcement is less than that of the model with normal strength reinforcement. At the conclusion of the test, only the upper end of the interior columns on the second story of TF-3 developed plastic hinges. Fig. 8 depicts the plastic hinge development condition and distribution patterns of the three frame models at selected inter-story drift angles. The overall conditions of the three frame models at termination of tests are shown in Fig. 9. Fig. 10 shows the horizontal load-average rotation relationship of beam end section 1 of the three test frame models. Note that in Fig. 10 the rotation of plastic hinge is expressed in radian, a dimensionless unit.

### 3.3 Horizontal load-displacement hysteretic curves

Horizontal load-displacement hysteretic curves of all three frame models are shown in Fig. 11. The frame models TF-1 and TF-2 had the same axial load ratio while different strength of reinforcing bars. Though high strength reinforcement was used, TF-2 was designed to have similar cross sectional capacity and stiffness to TF-1. The hysteretic loops of TF-1 are plumper than those of TF-2, indicating more plasticity was developed in TF-1. The residual deformation corresponding to total unloading of TF-2 are less than those of TF-1. TF-2 suffered from less severe damage to concrete and exhibited a higher elastic restoring capability owing to the use of high strength steel. Frame models TF-2 and TF-3 were both reinforced with HRB600 high strength steel but TF-3 had a higher axial load ratio. The hysteretic curves of TF-2 exhibited more serious pinching effect than TF-3, indicating that the axial load ratio has the same influence on the hysteretic behavior as frames with normal strength reinforcement. However, in the vicinity of the turning points from loading to unloading, the hysteretic curves of TF-3 are more abrupt than TF-3.

Horizontal load-displacement skeleton curves of the three frame models were obtained based on their hysteretic loops. The yield displacement  $\Delta_y$  of each model was calculated based on the equivalent energy method. The ultimate state of each model was assumed to be reached when the inter-story drift angle was  $1/25$ . Then the top displacement and inter-story drift angle corresponding to yield and ultimate states of each frame model can be obtained and listed in Table 4. It can be easily determined from Table 4 that the yield deformation of frame models with high strength reinforcement is noticeably larger than the one with normal strength reinforcement, implying that models TF-2 and TF-3 were later than TF-1 into inelastic range.

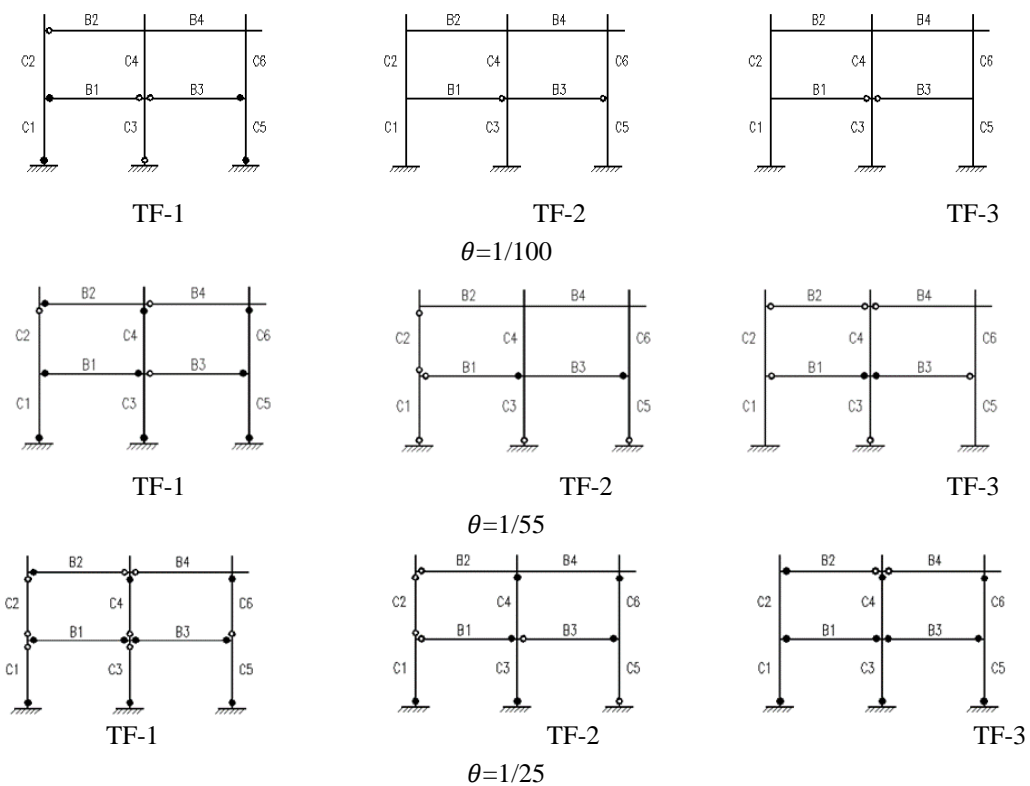


Fig. 8 Plastic hinge distribution of three specimens at different drift

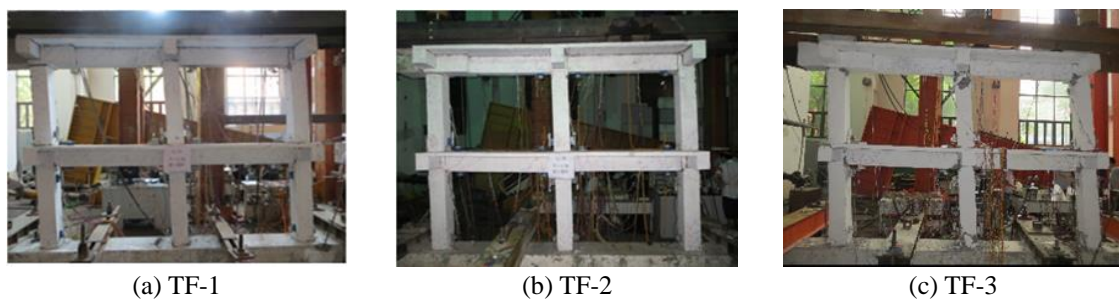


Fig. 9 Overall conditions of test frame models

When the inter-story drift angle reaches  $1/25$ , all the measured displacement ductility factors of TF-1 exceeded 5.0, and those of TF-2 and TF-3 were approximately 4.0. It is believed that the displacement ductility factors of TF-2 and TF-3 can exceed 4.0 when the load carrying capacities of the frame models drop below 85% of the peak values. If taking the displacement ductility factor as the ductility measure of frames, the frame reinforced with normal strength steel is more ductile than the one reinforced with high strength steel. It is worth noting, however, that the strength of frame model TF-2 and TF-3 didn't degrade significantly when the inter-story drift angle was up to  $1/25$  according to the skeleton curves of the two models, indicating the good deformation capacity of the frames with high strength reinforcement.

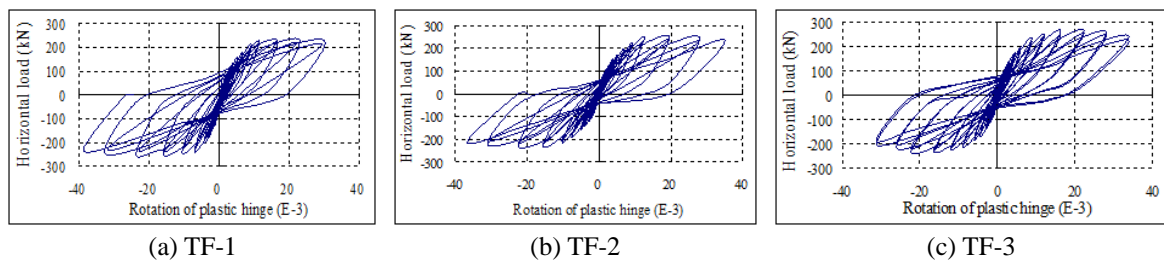


Fig. 10 Horizontal load-plastic hinge rotation at beam end section 1 of three frame models

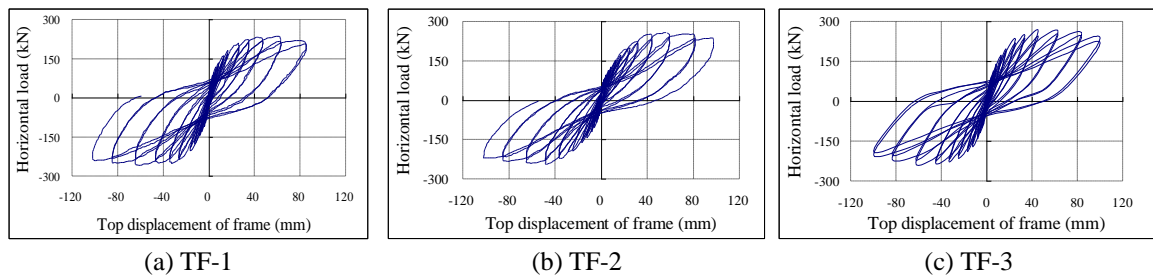


Fig.11 Horizontal load-top displacement hysteresis loops of three frame models

Table 4 Deformation and displacement ductility factor

Level	Identification	Disp. at yield (mm)	Drift ratio at yield	Max. disp. at 1/25 (mm)	Disp. ductility factor at 1/25
Top floor	TF-1	16.0	1/156	81.7	5.1
	TF-2	20.8	1/121	83.2	4.0
	TF-3	21.3	1/122	83.3	4.0
Inter-story drift of first story	TF-1	8.0	1/156	42.1	5.3
	TF-2	10.8	1/115	43.4	4.0
	TF-3	11.8	1/125	46.3	3.9
Inter-story drift of second story	TF-1	7.6	1/166	39.4	5.2
	TF-2	10.0	1/126	38.2	3.8
	TF-3	9.5	1/126	37.1	4.0

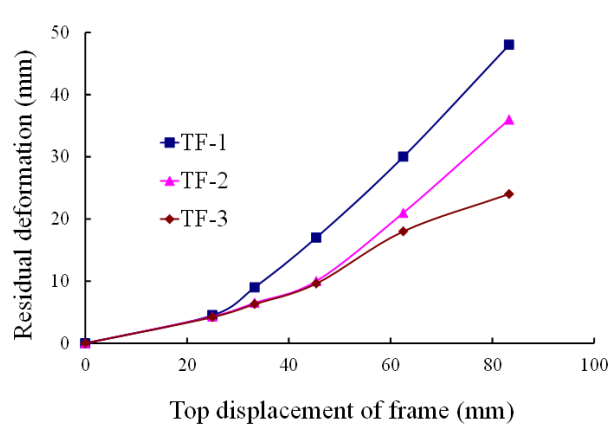
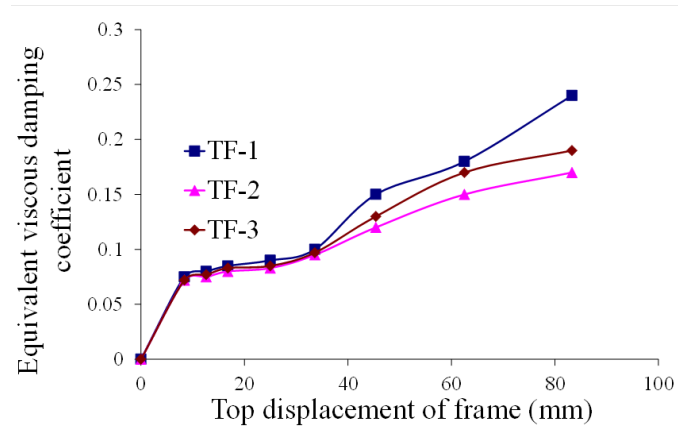


Fig. 12 Comparison of residual deformation value of specimens

Fig. 13 Comparison of  $h_{eq}$ 

### 3.4 Residual deformation and energy dissipation

The residual deformation versus lateral displacement curves of the three frame models are depicted in Fig. 12. Along with the increase of horizontal displacement, frame models are further into inelastic range and suffer from accumulated damages and residual deformation. Under the same axial load ratio, large residual deformation indicates high energy dissipation capacity, which can be demonstrated by the shape of hysteretic loops. Fig. 13 shows the equivalent viscous damping ratio  $h_{eq}$  versus lateral displacement curves. It is obvious that that the energy dissipation capacity of frame model with normal strength reinforcement is higher than that of frame models with high strength reinforcement.

## 4. Numerical simulation

It is necessary to evaluate the response characteristics of the test frame models using finite

element (FE) analysis in addition to experimental studies. Such FE nonlinear analysis can further reveal the mechanical behavior of the structure during its loading to failure based on advanced theories and numerical techniques. In the present study, the test frame models were analyzed using the proved-reliable nonlinear finite element software DIANA (2004) to verify the test results. Concrete members were simulated using two dimensional plane stress elements. The concrete material was considered based on nonlinear fracture mechanics to account for cracking. Plasticity theory was used for concrete in compression and reinforcing bars.

#### 4.1 Modeling of concrete

The numerical model of concrete is illustrated in Fig. 14. The cracking of concrete is modeled in accordance with a constant stress cut-off criterion, where a crack is assumed to be initiated perpendicular to the major principle stress if the concrete is subjected to stress in excess of its tensile strength. The ultimate crack width,  $w_u$ , is calculated using the fracture energy  $G_F$  and the tensile strength  $f_t$ . A three-point bending test according to the recommendation of RILEM 50-FMC (1985) was conducted to obtain the fracture energy  $G_F$  of concrete. The uniaxial tensile strength  $f_t$  was determined based on the compressive strength  $f'_c$

$$f_t = 0.3(f'_c)^{2/3} \quad (2)$$

Fig. 15 depicts the bilinear tensile stress-strain curve for the softening effect of concrete in tension after cracking where the maximum strain  $\epsilon_u^{cr}$  was taken as 0.001 (Li *et al.* 2009). The behavior of concrete in compression was simulated by an elasto-plastic model with its yield state limited by a Drucker-Prager yield surface. After yielding an isotropic hardening with an associated flow rule was used. The angle of internal friction of concrete is assumed to be  $30^\circ$ . The cohesion  $c$  used in the analysis is calculated by

$$c = f'_c(\epsilon_{uniaxial}^p)^{\frac{1-\sin\phi}{2\cos\phi}} \quad (3)$$

where  $f'_c(\epsilon_{uniaxial}^p)$  is the softening or hardening parameter as a function of the plastic strain in the direction of the uniaxial compression stress. The unloading and reloading behavior of the post peak responses using the initial elastic stiffness is shown in Fig. 14. A Poisson's ratio of 0.15 was used in the analysis.

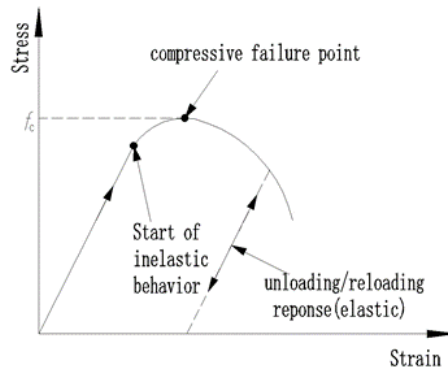


Fig. 14 Concrete in compression

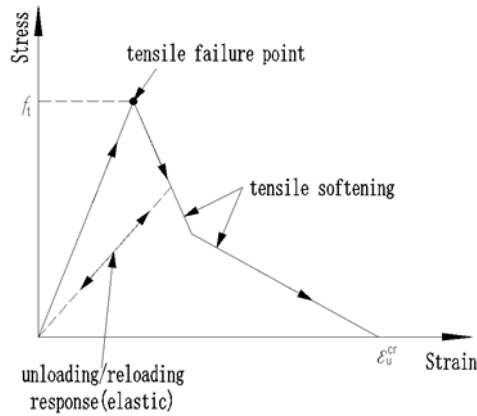


Fig. 15 Concrete in tension

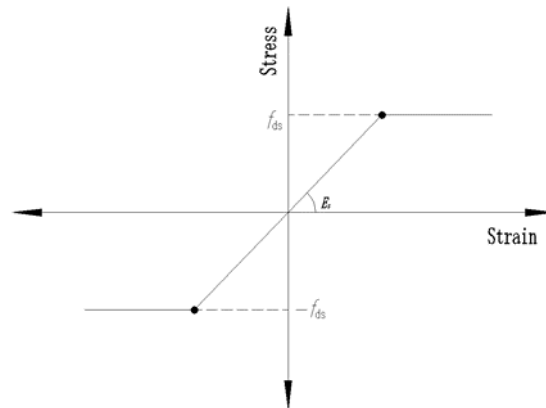


Fig. 16 Steel reinforcement

#### 4.2 Modeling of reinforcing bars

The reinforcing bars in the test frame models were modeled as separate truss elements in combination with interfacial elements to account for the interaction between the reinforcement and concrete. An elasto-plastic curve, as illustrated in Fig. 16, was used to define the stress-strain relationship of reinforcement. It is noted that the reinforcement at frame corners and exterior beam-column joints was modeled as straight rebars without the consideration of the bent portions for anchorage. Selected bond-slip relationship was directly assigned to the reinforcing bars.

#### 4.3 Bond slip consideration

The bond-slip law used in the numerical simulation is depicted in Fig. 17, which is based on CEB-FIP model code (1993). The set of equations of bond stress for different segments of the curve are described as follows:

$$\begin{aligned} \tau &= \tau_{max} \left(\frac{s}{s_1}\right)^\alpha & \text{for } 0 \leq s \leq s_1 \\ \tau &= \tau_{max} & \text{for } s_1 \leq s \leq s_2 \end{aligned}$$

$$\tau = \tau_{max} - (\tau_{max} - \tau_f) \frac{s - s_1}{s_2 - s_1} \quad \text{for } s_1 \leq s \leq s_2$$

$$\tau = \tau_f \quad \text{for } s_2 \leq s \leq s_3$$

where  $\tau$  is the bond stress;  $\tau_{max}$  is the bond strength;  $\tau_f$  is the residual bond stress;  $s$  is the relative slip between reinforcing bars and concrete;  $s_1$ ,  $s_2$  and  $s_3$  are characteristic slip values;  $\alpha$  is the an empirical coefficient. The parameters in the bond stress law depend on the reinforcing bar surface condition.

#### 4.4 Meshing of finite element model of test frames

The meshing of the finite element model is important to the analysis. Although a more refined meshing, indicating a larger number of elements, can result in analysis results with better accuracy, the computation will be more costly, or even cause difficulty in convergence. In the present study, the clear span and cross section depth of beam were equally divided into 20 and 5 segments with 70 mm and 50 mm segment lengths respectively. The clear height and cross section depth of column were equally divided into 10 and 5 segments with 100 mm and 40 mm segment lengths respectively. Although the element size can be further reduced to obtain a more refined meshing scheme, no obvious difference would be led to.

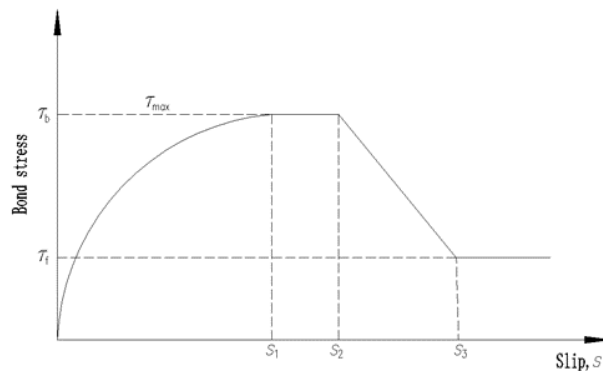


Fig. 17 Bond-slip law

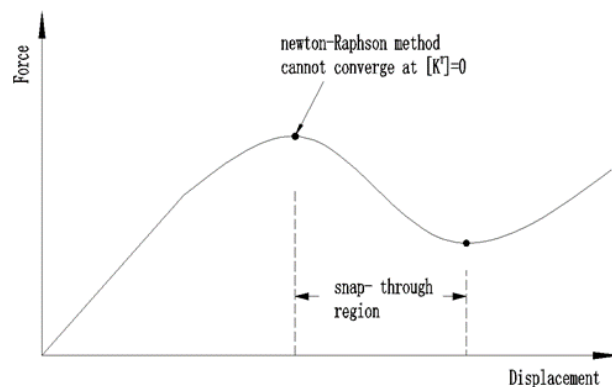


Fig. 18 Snap-through effect

#### 4.5 Solution algorithm

The Newton-Raphson method was applied at the early loading stage to solve the nonlinear equations. Then arc-length technique combined with the line search method was followed to locate the descending part of the post peak behavior and snap-through phenomenon as shown in Fig. 18. A maximum limit of 50 iterations was used for convergence and the tolerance was taken as 0.001. The analysis results indicated the appropriateness of convergence criterion. All the test frame models were applied in accordance with the loading sequence as shown in Table 2.

#### 4.6 Comparison of simulated and experimental load-displacement behavior

Comparison of the numerical simulation and experimentally obtained results in terms of horizontal load- displacement skeleton curves and hysteretic loops is shown in Fig. 19. The finite element simulation of frame model TF-1 had a good agreement with the experimental responses, as shown in Fig. 19. Judging from the skeleton curves, the predicted responses corresponding to a few initial cycles were very close to the experimental ones, though the later predictions were slightly lower after the frame model entered inelastic range. The predicted hysteretic loops showed very good agreement in terms of the unloading and reloading paths with the experimental responses. Fig. 20 depicts the comparison of finite element simulation and experimental results for frame model TF-2. The predicted skeleton curve underestimated the horizontal loads of the frame after yielding with a 12% error for the peak horizontal load. The hysteretic responses demonstrated a good agreement for the unloading and reloading branches between the simulated and observed results. The comparison of numerical and experimental results for frame model TF-3 was shown in Fig. 21. The finite element numerical analysis seemed have predicted a good response with respect to the initial loading cycles. The prediction of horizontal loads after yielding was much improved compared with frame models TF-1 and TF-2. The predicted hysteretic behavior exhibited slightly deviation for the unloading especially for the cycles when significant plasticity had developed. The reloading branches were still very well simulated according to the comparison. It can be seen that the finite element analysis can yield a good prediction with respect to the load-displacement behavior of the frame models with various strength reinforcements.

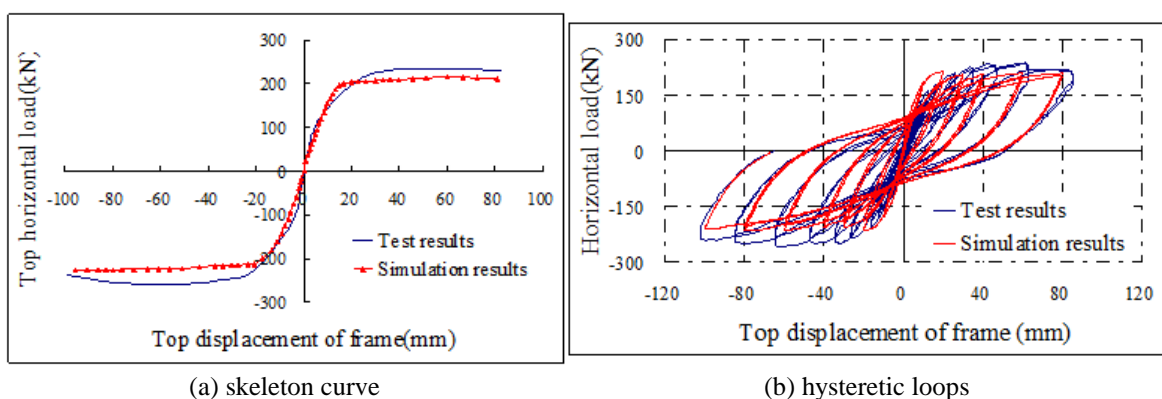


Fig. 19 Comparison of numerical and experimental results of TF-1

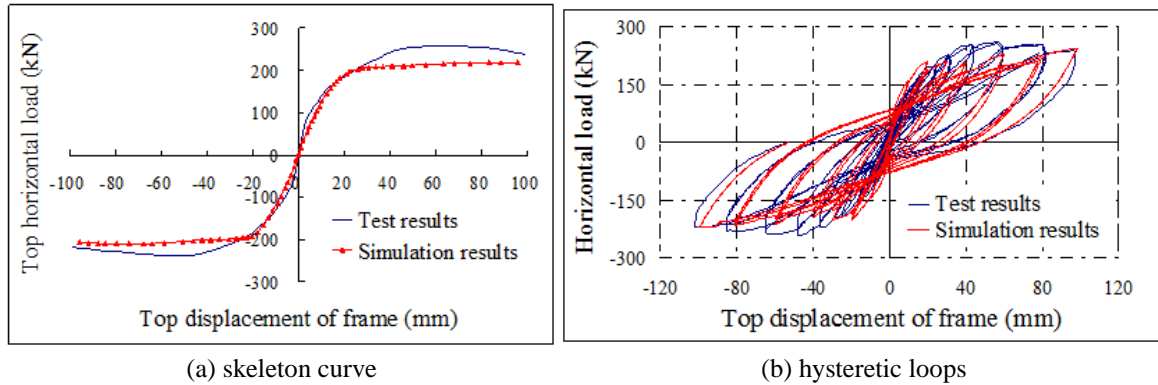


Fig. 20 Comparison of numerical and experimental results of TF-2

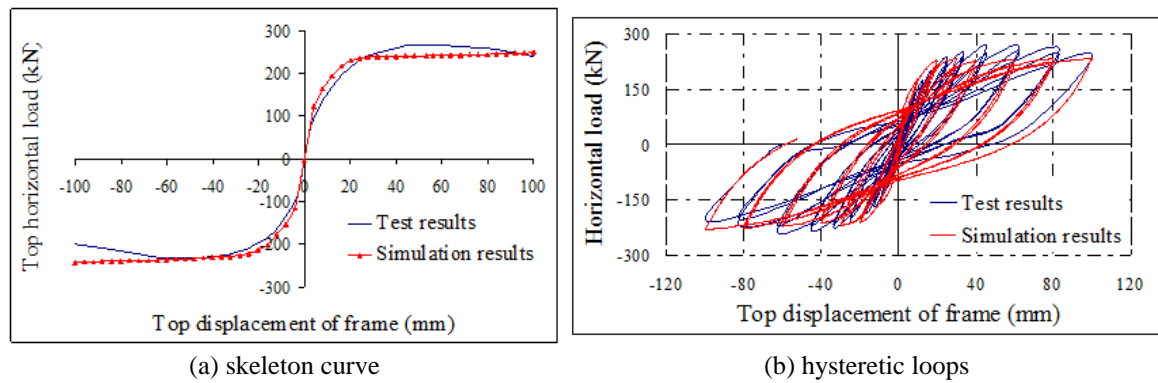


Fig. 21 Comparison of numerical and experimental results of TF-3

## 5. Conclusions

1) Compared with frames with normal strength reinforcement, frames with high strength reinforcement develop less plasticity at the same lateral displacement level due to the high yield stress of steel. However, the frames with high strength reinforcement exhibit better elastic restoring performance and less residual deformation, which is an advantage for post-quake rehabilitation.

2) If the equivalence of strength principle is followed in the design, the load carrying capacities and their degradation characteristics of the frames using normal and high strength reinforcement are very similar. Since the lateral displacement at yield of frames with high strength reinforcement is much larger than that of frames with normal strength reinforcement, the frames with normal reinforcement are more ductile than those with high strength reinforcement if the displacement ductility coefficient is used as the ductility measure. However, the post yield deformation capacity of the frames with high strength reinforcement is as good as that of the normal frames. Thus if using the overall deformation capacity as the measure of ductility, frames with high strength reinforcement have comparable ductility characteristics with normal frames.

3) The hysteretic loops of frames with high strength reinforcement are slimmer than those of the frames with normal reinforcement, resulting in less amount of energy dissipation during the

test. The frames with normal reinforcement dissipate earthquake induced energy by inelastic deformation while frames with high strength reinforcement dissipate less amount energy due to the high level of yielding stress of the high strength steel. In frames with high strength reinforcement, a higher axial load ratio can lead to the delay the cracking of columns. In addition, a reasonable plastic pattern can form where column ends hardly develop plastic hinges except for the bottom story column ends.

4) The simulation results of the test frames using the proved-reliable finite element program DIANA show a good agreement with the test results, indicating that the modeling and analysis techniques described in this paper can be satisfactorily adopted to study the behavior of concrete moment frames with high strength reinforcement.

### Acknowledgements

This research project is financially sponsored by the National Science Foundation of China under the grant number of 51478063 and the Fundamental Research Funding for Central Universities under the grant number of 106112014CDJZR200002. The authors would like to express their sincere thanks and appreciation to the various supporting agencies.

### References

- AASHTO (2012), *AASHTO LRFD bridge design specifications*, (6th Edition), American Association of State Highway and Transportation Officials, Washington DC.
- AASHTO (2013), *Interim revisions to the AASHTO LRFD bridge design specifications*, (6th Edition), American Association of State Highway and Transportation Officials, Washington, DC.
- ACI 318 Committee 318 (1971), *318-71: Building code requirements for reinforced concrete*, American Concrete Institute, Farmington Hills, MI.
- ACI 318 Committee 318 (2011), *318-11/318-11R: Building code requirements for reinforced concrete and commentary*, American Concrete Institute, Farmington Hills, MI.
- CEB-FIP Model Code 90 (1993), *CEB Bulletin No. 213/214*, Thomas Telford, Lausanne, Switzerland.
- Civil and structural groups of Tsinghua University, Xi'an Jiaotong University and Beijing Jiaotong University (2008), "Analysis on seismic damage of buildings in the Wenchuan Earthquake", *J. Build. Struct.*, **29**(4), 1-9.
- DIANA Version 9 (2004), *Finite element analysis user's manual-nonlinear analysis*, TNO Building and Construction Research, Delft, the Netherlands.
- Fu, J.P., Yang, H., Huang, Q. and Xue, F. (2014), "Nonlinear dynamic response of frame structures reinforced with high-strength steel bars under strong earthquake action", *J. Build. Struct.*, **35**(8), 23-29.
- GB 500010 (2010), *Code for design of concrete structures*, Ministry of Housing and Urban-rural Development, Beijing, China.
- GB 500011 (2010), *Code for seismic design of buildings*, Ministry of Housing and Urban-rural Development, Beijing, China.
- Harries, K.A., Shahrooz, B.M. and Soltani, A. (2012), "Flexural crack widths in concrete girders reinforced with high-strength reinforcement", *J. Bridge Eng.*, **17**(5), 804-812.
- Li, B., Kulkarni, S.A. and Leong, C.L. (2009), "Seismic performance of precast hybrid-steel concrete connections", *J. Earthq. Eng.*, **13**(5), 667-689.
- Mast, R.F., Dawood, M., Rizkalla, S.M. and Zia, P. (2008), "Flexural strength design of concrete beams reinforced with high-strength steel bars", *ACI Struct. J.*, **105**(4), 570-577.

- Rautenberg, J.M., Pujol, S., Tavallali, H. and Lepage, A. (2012), "Reconsidering the use of high-strength reinforcement in concrete columns", *Eng. Struct.*, **37**(1), 135-142.
- RILEM 50-FMC Committee (1985), "Determination of the fracture energy of mortar and concrete by means of three point bend tests on notched beams", *Mater. Struct.*, **18**(4), 287-290.
- Shahrooz, B.M., Reis, J.M., Wells, E.L., Miller, R.A., Harries, K.A. and Russell, H.G. (2013), "Flexural members with high-strength reinforcement: behavior and code implication", *J. Bridge Eng.*, **19**(1), 1-7.
- Wang, X.F. (2013), "Study on seismic performance of concrete frame structure reinforced with high-strength rebars", Ph.D. Dissertation, China Academy of Building Research, Beijing, China.

CC